ACS Catalysis

Open Access

This article is licensed under CC-BY 4.0

pubs.acs.org/acscatalysis

Research Article

Copper(I) Oxo Species in Cu/ZnO Catalysts and Its Role in the Methanol Synthesis from CO_2 Hydrogenation

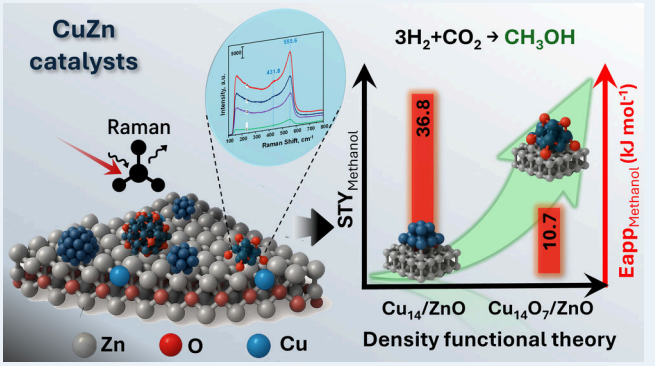
J. Soriano,[‡] Y. Fo,[‡] D. Gómez, J.M. López Nieto, A. Roy, R. Manzorro, R. Arenal, J.J. Calvino, W. Song, and P. Concepción*

Cite This: *ACS Catal.* 2026, 16, 11604−11617

Read Online

ACCESS | Metrics & More | Article Recommendations | Supporting Information

ABSTRACT: This study reveals the presence of low-atomicity copper(I) oxo clusters strongly anchored to ZnO in commercial-type Cu/ZnO catalysts that, coexisting with metallic copper nanoparticles, play a critical role in CO_2 hydrogenation. Their detection is challenging because metallic copper nanoparticles dominate the catalyst surface and these clusters appear in low amounts. Nevertheless, definitive evidence of their existence comes from the combination of *in situ* Raman spectroscopy, temperature-programmed CO surface reaction (TPSR-CO), time-resolved kinetic studies, and advance microscopy studies (STEM-XEDS and STEM-EELS). Catalytic studies combined with density functional theory (DFT) calculations demonstrate its critical role in methanol production and their size-dependent contribution to the total activity compared to traditional Cu-ZnO interfacial sites. According to DFT studies, CO_2 adsorption is significantly more favorable on small $Cu_{14}O_7$ and $Cu_{32}O_{16}$ clusters than on extended Cu_2O (111) (110) facets, metallic copper, or conventional metal-support interfacial sites. Moreover, the stabilization of carboxyl rather than formate-like intermediates follows a similar trend than the methanol production, being preferential on small $Cu_{14}O_7$ and $Cu_{32}O_{16}$ clusters, underlying a carboxyl-type intermediate path in methanol production.



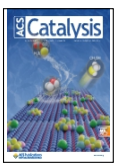
KEYWORDS: *CO_2 hydrogenation, Cu/ZnO, methanol, copper oxo clusters, Raman spectroscopy*

INTRODUCTION

The development of new technologies that meet efficiency and sustainability criteria is essential to address the growing demand for methanol, which is expected to exceed 500 million tons by 2050. Methanol synthesis from CO_2 using renewable hydrogen offers a more sustainable alternative to the current industrial process, but thermodynamic and kinetic restrictions significantly limit its industrial applicability. Furthermore, the lack of a deep understanding of the ultimate structural features controlling the performance of active sites in commercial catalysts remains a major bottleneck in developing novel catalysts. Since the intrinsic complexity of industrial catalysts is the major factor hindering a detailed analysis, most studies have focused on model catalysts, providing valuable descriptors for catalytic activity.[1−3] However, the presence of coexisting multiple species, some potentially inactive or exhibiting varying intrinsic activities, strongly affects the establishment of reliable atomic-level structure−activity correlations.

Cu/ZnO-based catalysts are used in commercial methanol synthesis from syngas, and widely explored for the alternative CO_2 hydrogenation process to methanol synthesis. Despite extensive research using a variety of operando spectroscopic techniques and theoretical analyses, the exact nature of active sites in Cu/ZnO catalysts for methanol synthesis remains elusive.[4] Various types of species have been proposed, such as Zn-doped Cu sites,[5] CuZn alloys,[6,7] Cu-ZnO interfaces,[8−12] Cu and ZnO crystal faces, Cu crystal steps, and Cu^+ sites,[13,14] among others.[15−18] While a clear consensus exists on the coexistence of copper in different oxidation states (Cu^+ and Cu^0), usually determined from X-ray photoelectron and Auger spectroscopies (XPS-AES), the exact nature of the Cu^+ species remains uncertain. Regarding the atomicity of copper sites, in recent studies done on model catalysts with controlled copper loadings, single isolated copper sites have been reported as the active site for methanol production, while small copper metal clusters or nanoparticles have been proposed as responsible for CO formation.[19−24] In contrast, in another study, Vajda et al.,[25] using a mass selected cluster deposition method of Cu_3, Cu_4, and Cu_{20}

Received: April 18, 2026
Revised: May 21, 2026
Accepted: May 21, 2026
Published: June 4, 2026



ACS Publications

© 2026 The Authors. Published by American Chemical Society

Downloaded from pubs.acs.org/acscacs/article-pdf/16/12/11604/6430569/cs-2026-029073.pdf by CADIZ UNIV user on 22 October 2026

clusters on an amorphous Al_2O_3 thin film, identified ultrasmall metallic Cu clusters as responsible for methanol production, with Cu_4 clusters being the most active one for methanol production compared to Cu_3 and Cu_{20}. However, the identification of these copper clusters in industrially relevant catalysts is a challenge, because of the high copper loading (usually 50−60 wt %) and the dominance of metallic copper species, where the coexistence of these clusters is over-hidden, escaping the detection limit of many spectroscopic tools. To this, it is necessary to add their potential dynamic evolution under reaction conditions. As a result, the incomplete understanding of active sites leads to conflicting and controversial findings.

In this context, this study delves into the intricate nature of active sites in commercial Cu/ZnO methanol catalysts. Through the combination of *in situ* characterization techniques, we have successfully identified highly dispersed copper(I) oxo species in the cluster and atomic range strongly interacting with the ZnO support. These species, coexisting with metallic copper nanoparticles, play a critical role in CO_2 hydrogenation. Our findings, supported by *in situ* Raman, *in situ* electron microscopy, time-resolved kinetic studies, and density functional theory (DFT) calculations, provides a deeper understanding of the contribution of these copper(I) oxo clusters and atomic structures on the overall methanol production.

In definitive, this work underscores the complexity of commercial-like Cu/ZnO catalysts, where additional species, not yet considered, may co-exist and potentially account for the so-called "synergetic effect of ZnO".

RESULTS AND DISCUSSION

Cu/ZnO Synthesis

In this study, a series of Cu/ZnO catalysts with a Cu/Zn molar ratio of 70/30 were prepared by a co-precipitation method at a controlled pH of around 6.5, using a variety of precipitating agents, including ammonium bicarbonate, sodium hydroxide, and ammonium hydroxide, and at different rates, ranging from 0.25 to 1 mL min^{-1} (details in Experimental Methods). After synthesis, all samples underwent a calcination process at 360 °C for a duration of 9 h. Subsequently, they were subjected to a reduction treatment in hydrogen gas at 200 °C for 3 h. For ease of identification, the synthesized catalysts were named using a systematic nomenclature: CuZn-X−Y, where X represents the specific precipitating agent used and Y denotes the corresponding addition rate.

Comprehensive physicochemical characterization was performed on the prepared catalysts (Figures S1−S12 and Tables S1−S3). The results summarized in Figure 1a,b indicate changes in the surface area of the catalysts with the higher values for samples prepared with ammonium bicarbonate as a precipitating agent (i.e., 39 m^2 g^{-1}), in line with previous reports in the literature.[26] The basic properties of the samples are analyzed from TPD of CO_2 analysis (Figure S12), showing in all cases sites of medium CO_2 interaction strength, which corresponds with CO_2 desorption in the 200−450 °C range. For reduced samples, the average size of the copper particles determined by X-ray diffraction (XRD) measurements, including Scherrer equation analysis, revealed that they fell within the range of 25 to 15 nm in all samples, above the critical value of 10 nm reported for catalytic activity (Table S1).[27] Similar Cu particle sizes have been determined from high-resolution transmission electron microscopy (HRTEM) analysis done for example on the CuZn-NaOH-0.25 sample (Figure S10). In addition to these results, from the XPS data presented in Table S2, the presence of both zinc oxide and Cu^0, with similar binding energies (BE) (i.e., 1022.0 eV for ZnO and 932.6 eV and modified auger parameter (α') =1851.1eV for Cu), was observed on all the reduced and reacted catalysts. A careful analysis at the $ZnL_3M_{4,5}M_{4,5}$ auger line rules out the formation of surface CuZn alloyed species (Figure S6) in the samples exposed to reaction conditions, as indicated by the absence of a shoulder at 991.6 eV.[6,28] Additionally, XPS analysis in the Na 1s region did not reveal any detectable Na signal within the detection limit of the technique (Figure S8), ruling out the presence of residual sodium species after synthesis and washing procedures. Regarding the surface molar ratio of copper and zinc, a higher Zn/Cu ratio compared to the bulk composition of the catalysts was observed in all samples. This enrichment in zinc at the catalyst surface was further enhanced after subjecting the catalysts to hydrogen reduction and exposure to reaction conditions in a high-pressure catalytic reactor connected to the XPS chamber (Table S2), a behavior also reported in the literature.[9] Nevertheless, if comparing under the same activation conditions, then the Zn/Cu atomic ratio indicates not relevant differences among the samples (Figure S7). According to the literature, a critical point in methanol synthesis is the stabilization of Cu^+ species.[13,29,30] However, no clear information could be retrieved by XPS-AES analysis (Figure S5), where the absence of a clear component at 916.5 eV at the Cu-$L_3M_{4,5}M_{4,5}$ auger line makes the identification of Cu^+ species questionable. To this, we have to add the limited IR sample transparency and considerable background noise, constraining the infrared (IR) studies of adsorption of CO as a probe molecule for identification of Cu^+ sites.[31]

Catalytic Studies

The samples were evaluated in the CO_2 hydrogenation at 20 bar with a CO_2/H_2 ratio of 1:3, at varying temperatures and space velocities (Tables S4 and S5, respectively). Across all conditions, CO_2 conversion and methanol yield increased with temperature, with CuZn-NH_4HCO_3 exhibiting the highest catalytic activity, in line with their larger surface area. Given the direct relationship between catalyst surface area and activity, methanol production was normalized by the surface area of each catalyst to enable a direct comparison of catalytic activity. Hence, the initial rates of methanol formation in mmol h^{-1} m^{-2} are compared in Figure 1c, displaying the highest methanol formation rate for the CuZn-NaOH-0.25 sample while the lowest for CuZn-NH_4HCO_3, whereas the initial rate of CO formation remained relatively consistent across all co-precipitated catalysts. These findings align with the apparent activation energy for methanol and CO production, as shown in Figure 1d. The CuZn-NaOH-0.25 sample exhibited lower apparent activation energies for both methanol (11 kJ mol^{-1}) and CO (84 kJ mol^{-1}) compared to CuZn-NH_4HCO_3 (17 and 111 kJ mol^{-1}, respectively) (Table S8), and in both cases lower than typically reported for CuZn systems (∼33−65 kJ mol^{-1} for methanol and ∼80−120 kJ mol^{-1} for CO).[32−35] These results suggest a modification of the active sites, the reaction mechanism, or the adsorption strengths of key intermediates involved in methanol and CO production on the co-precipitated samples, with methanol production being favored on the CuZn-NaOH-0.25 sample compared to CuZn-NH_4HCO_3. Furthermore, intrinsic methanol formation activity normalized to surface copper species determined by N_2O-TPR (Table S7) shows the highest reactivity on the CuZn-NaOH-0.25 sample. Consequently,

Downloaded from pubs.acs.org/acscats/article-pdf/16/12/11604/6430569/cs-2026-029073.pdf by CADIZ UNIV user on 22 October 2026

https://doi.org/10.1021/acscatal.6c02907
ACS Catal. 2026, 16, 11604−11617

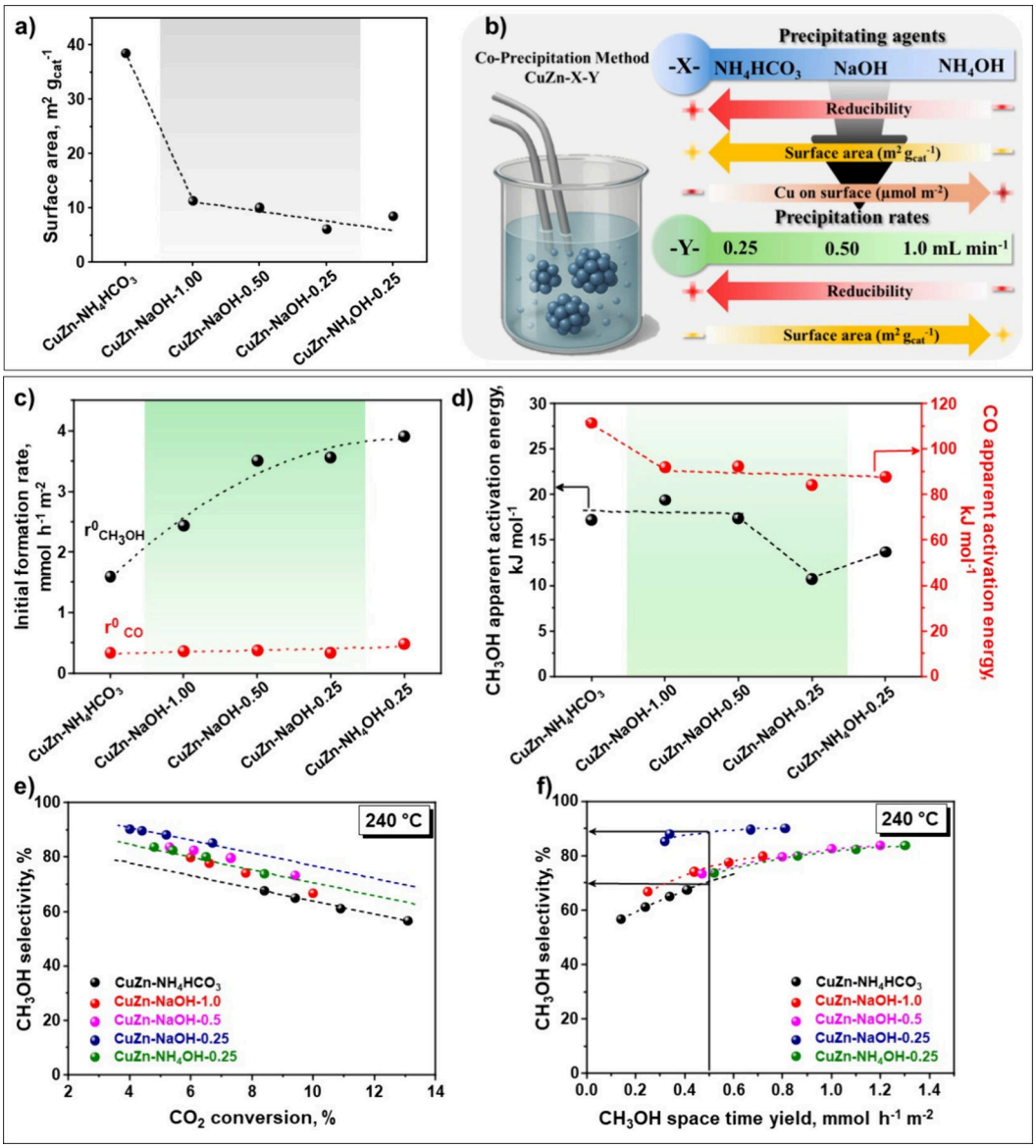


Figure 1. Physicochemical properties. (a) Surface area as a function of the precipitating agent and the rate. (b) Schematic effect of the precipitating agent and rate on the physicochemical parameters of CuZn-X−Y catalysts. Catalytic performance of CuZn-X−Y catalysts in the CO_2hydrogenation at 20 bar. (c) Initial reaction rate of methanol and CO formation (in mmol h^{-1} m^{-2}) at 240 °C. (d) Apparent activation energy (in kJ mol^{-1}) for methanol and CO formation. (e) Variation of the selectivity to methanol with the CO_2 conversion at 240 °C. (f) Selectivity to methanol versus the production of methanol (i.e., CH_3OH space time yield, in mmol h^{-1} m^{-2}) at 240 °C. Experimental conditions detailed in Tables S4 and S5.

the CuZn-NaOH-0.25 sample demonstrated higher selectivity toward methanol at iso-conversion, as illustrated in Figure 1e. For instance, at 9.3% CO_2 conversion, 240 °C, and 20 bar, the CuZn-NaOH-0.25 sample achieved a methanol selectivity of 80.5%, compared to only 65.3% for CuZn-NH_4HCO_3. This trend is further emphasized when comparing methanol selectivity at a constant methanol production rate (Figure 1f). The CuZn-NaOH-0.25 catalyst exhibited a promising selectivity of 89.5% at a methanol production rate of 0.5 $mmol_{MeOH}$ h^{-1} m^{-2}, while CuZn-NH_4HCO_3 showed a lower selectivity to methanol (ca. 69.4%).

Additional catalytic studies at 1 bar showed, despite the inherent higher CO production due to thermodynamic aspects, a higher methanol selectivity on the CuZn-NaOH-0.25 catalyst than on CuZn-NH_4HCO_3 (with values of 76.7 and 55.3%, respectively), at 0.45% CO_2 conversion and 200 °C (Figure S15 and Tables S9 and S11), following the same trend as observed at 20 bar.

These differences in catalytic performance among the samples are difficult to determine based on the physicochemical properties of the catalysts, due to their similarity in Cu particle size (for instance between CuZn-NaOH-0.25 and CuZn-NH_4HCO_3), basic properties as determined by TPD-CO_2, surface composition of Cu and Zn determined by XPS (where under reaction conditions the Zn/Cu is between 1.2 and 1.6), and chemical state of surface elements (being Cu^0 and ZnO the only detected elements). Nevertheless, markedly different H_2-TPR profiles (Figure S11) have been observed between the samples. Particularly, a broad reduction peak shifted to higher temperatures

https://doi.org/10.1021/acscatal.6c02907
ACS Catal. 2026, 16, 11604−11617

Downloaded from pubs.acs.org/acscacs/article-pdf/16/12/11604/6430569/cs-2026-029073.pdf by CADIZ UNIV user on 22 October 2026

is observed on samples precipitated with NaOH and NH_4OH, revealing heterogeneity in copper species and the existence of strong metal−support interactions. In contrast, a much narrower peak is observed at lower temperatures in the CuZn-NH_4HCO_3 sample, indicating the presence of more reducible Cu species in this sample. The variety of copper species suggested by the multiple reduction events on the H_2-TPR profile was not corroborated by XRD or XPS analysis, where copper metal nanoparticles were detected as the only species present in the reduced samples.

Interestingly, Raman spectroscopic studies done on selected samples (Figure 2 and Figure S17) (i.e., CuZn-NH_4HCO_3, CuZn-NaOH-0.25, and CuZn-NH_4OH-0.25), after *in situ* reduction at 200 °C, revealed a characteristic Cu_2O-like vibrational feature associated with highly dispersed small Cu(I) oxo clusters, with a strong band at ∼573 cm^{-1} together with less intense ones at 438 and 230 cm^{-1}.[36−39] Further evidence of the stabilization of this entity comes from the reddish colour of the co-precipitated samples after H_2 reduction characteristic of Cu_2O (Figure S3). By further increasing the temperature in inert atmosphere up to the reaction temperature (260−280 °C), the main peak of the co-precipitated samples reduces its intensity and shifts due to thermal effects to ∼559 cm^{-1} (Figure S17). However, after exposure to reaction conditions (CO_2+H_2, 260−280 °C; 1 bar), the initial bands at 559, 438, and 230 cm^{-1} restore in intensity and remain practically constant during the experiment (Figure 2, spectra a, b, and c, and Figures S17 and S18). These results point to the existence of highly dispersed small Cu(I) oxo clusters under reaction conditions in the co-precipitated samples. The absence of full oxidized CuO species is supported by the lack of its characteristic peak at 632 cm^{-1}. The fact that Cu_2O is observed by Raman spectroscopy and not by other techniques, such as XRD and XPS-AES, is related to the higher sensitivity of the former, and its existence as a minority, highly dispersed specie probably in the form of subnanometer-sized Cu(I) oxo clusters, being below the detection limit of the other techniques.

To obtain further information of these ensembles, temperature-programmed CO surface reaction (TPSR-CO) is used as test reaction analyzing the reactivity of these Cu(I) oxo

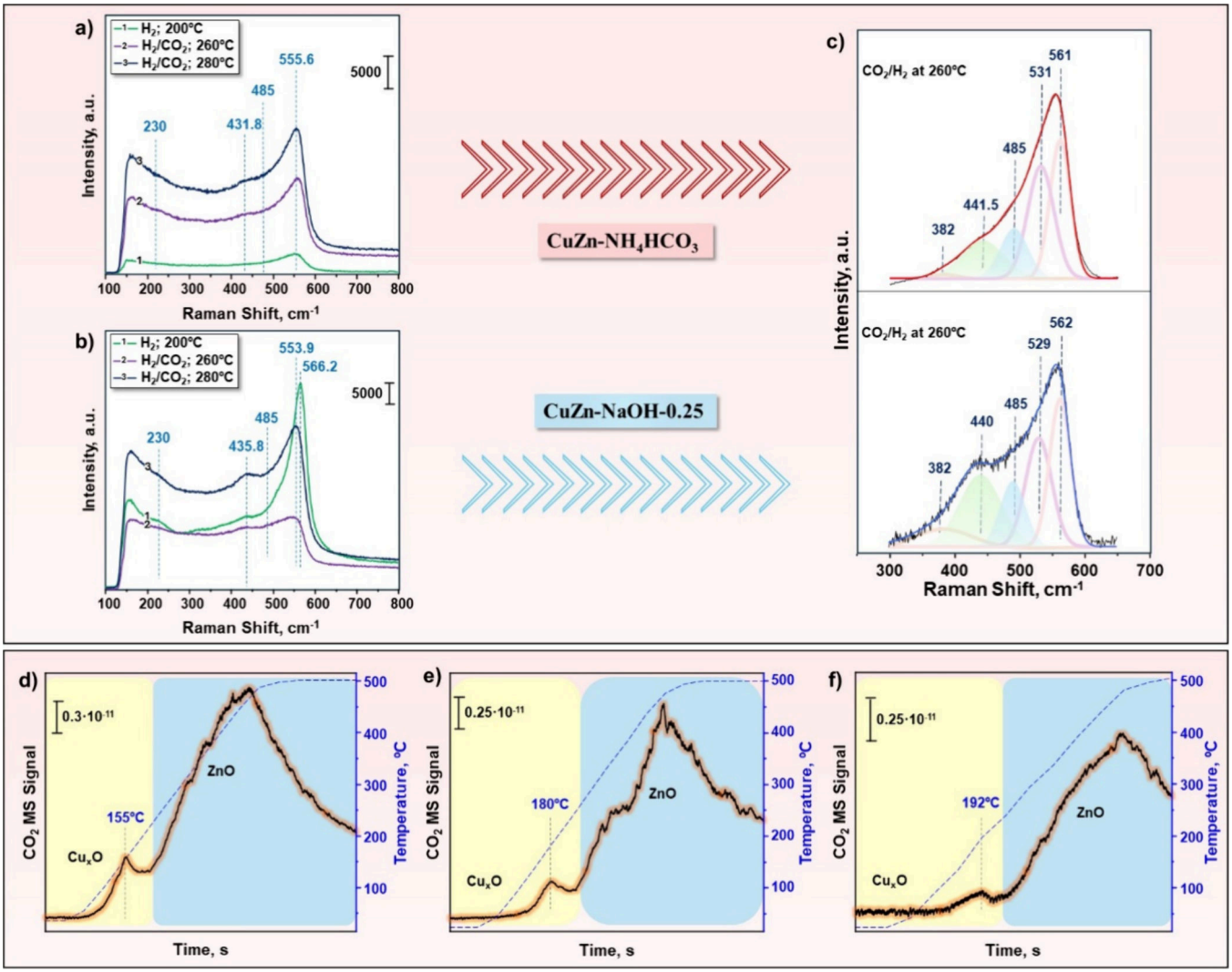


Figure 2. Spectroscopic and chemical evidence of the coexistence of small Cu(I) oxo domains. *In situ* Raman spectra under H_2 and in CO_2 hydrogenation conditions (H_2/CO_2 = 3 and 1bar) in the 260−280 °C temperature range on the (a) CuZn-NH_4HCO_3, (b) CuZn-NaOH-0.25, and (c) deconvoluted spectra of CuZn-NH_4HCO_3 vs CuZn-NaOH-0.25 samples under H_2/CO_2 at 260 °C. TPSR-CO following CO_2 evolution by MS (m/z = 44) on (d) CuZn-NH_4HCO_3, (e) CuZn-NaOH-0.50, and (f) CuZn-NaOH-0.25 samples.

https://doi.org/10.1021/acscatal.6c02907
ACS Catal. 2026, 16, 11604−11617

Downloaded from pubs.acs.org/acscacs/article-pdf/16/12/11604/6430569/cs-2026-029073.pdf by CADIZ UNIV user on 22 October 2026

domains in the CO oxidation to CO_2, which is monitored by online mass spectrometry (MS). This reactivity can be correlated with their size, dispersion, and interaction with the support.[40−44] In these studies (experimental details in the Supporting Information (SI)), a broad peak of CO_2 formation is observed at temperatures above 250 °C in all samples, as in pure ZnO (Figure S21). This is associated with the removal of surface oxygen species of ZnO. In the low-temperature range, no peaks are observed in pure ZnO, while a peak with a maximum at 155 °C is observed in the CuZn-NH_4HCO_3 sample (Figure 2d), which shifts to a higher temperature, 180 °C, in the CuZn-NaOH-0.5 (Figure 2e) and 192 °C in the CuZn-NaOH-0.25 samples (Figure 2f). This peak is likely attributable to the presence of highly dispersed small Cu(I) oxo clusters displaying Cu_2O-like vibrational features, which exhibit higher reactivity toward CO oxidation than bulk Cu_2O (with a peak at 293 °C, Figure S22).[42] The progressive shift of the CO oxidation peak toward higher temperatures (155 to >192 °C) correlates with cluster size reduction, as smaller clusters have stronger ZnO anchoring and higher activation energy for CO oxidation.[45] Based on it, the following trend in cluster size can be expected, CuZn-NH_4HCO_3 > CuZn-NaOH-0.5 > CuZn-NaOH-0.25. Under reaction conditions, a broadening of the Raman band with the formation of an additional new band at ∼485 cm^{-1} and an increase in the intensity of the 440 cm^{-1} component is observed, being more pronounced in the CuZn-NaOH-0.25 sample than in the CuZn-NH_4HCO_3 one (Figure 2b,c and Figure S18B). This new band at 485 cm^{-1} together with the 440 cm^{-1} band is ascribed to Cu-OH species (reference in Figure S16B),[37] which may be formed and stabilized under reaction conditions due to the coproduction of water and become stabilized preferentially on the small copper oxo clusters rather than on the bigger ones. This is consistent with DFT studies performed by Mikosch et al.[46] on $Cu_{14}O_7$ and $Cu_{32}O_{16}$ nanoclusters.

The coexistence of the aforementioned copper(I) oxo clusters is confirmed by scanning TEM (STEM) analytical studies. STEM X-ray energy-dispersive spectroscopy (XEDS) elemental maps (Figure S24), which depict the spatial distribution of Cu and Zn phases, reveal an intimate mixing of Cu-based and ZnO particles in the *ex situ* reduced CuZn-NaOH-0.25 sample. Notably, while not apparent from the chemical map, the integrated spectrum over a ZnO crystal surface (orange rectangle in Figure S24A) unveils a Cu peak, suggesting the presence of highly dispersed, potentially nanostructured Cu-based species on the ZnO surface (Figure S24B). Directly visualizing these surface features using HRTEM or high-angle annular dark-field (HAADF)-STEM imaging is challenging due to the similar atomic masses and numbers of Cu and Zn. Moreover, this surface Cu species could extend from cluster to atomic dimensions, explaining its absence in HRTEM images. Electron energy-loss spectroscopy (EELS)-STEM analysis (Figure S24C−F) complements XEDS-STEM measurements, providing insights into the spatial distribution and oxidation state of Cu-containing phases. A detailed analysis of the energy-loss near-edge structure (ELNES) of the Cu-$L_{2,3}$ edge reveals the coexistence of Cu(II) and Cu(I) within the sample and in close contact with the ZnO surface (Figure S24D). Multiple linear least-squares (MLLS) fitting applied to this EELS dataset[47] allowed to accurately map the distribution of these two Cu oxidation states. Well-defined, larger Cu-containing crystals predominantly correspond to CuO, while the Cu(I)-rich structure overlaps significantly with the spatial distribution of Zn (Figure S24F). The presence of CuO arises from the exposure of *ex situ* reduced samples to air, as confirmed by Raman studies conducted after air exposure and disappearing after *in situ* H_2reduction (see Figure S17).

In situ STEM-EELS experiments have put forward the evolution of the Cu-based phases, where the CuZn-NaOH-0.25 sample was subjected to a reducing atmosphere (50% H_2, 50% N_2) at 200 °C (Figure 3a−c). Data clustering analysis of the EELS dataset revealed the spatial distribution of the primary components, indicating that CuO particles were reduced to metallic Cu (purple). However, ZnO particles (yellow) were partially decorated with a mixed CuZn feature (orange), corresponding to highly dispersed Cu structures. This Cu closely linked to the Zn signal, also observed in the *ex situ* experiments, can be attributed to the Cu(I) oxo clusters identified by Raman spectroscopy and corroborate the TPSR-CO studies.

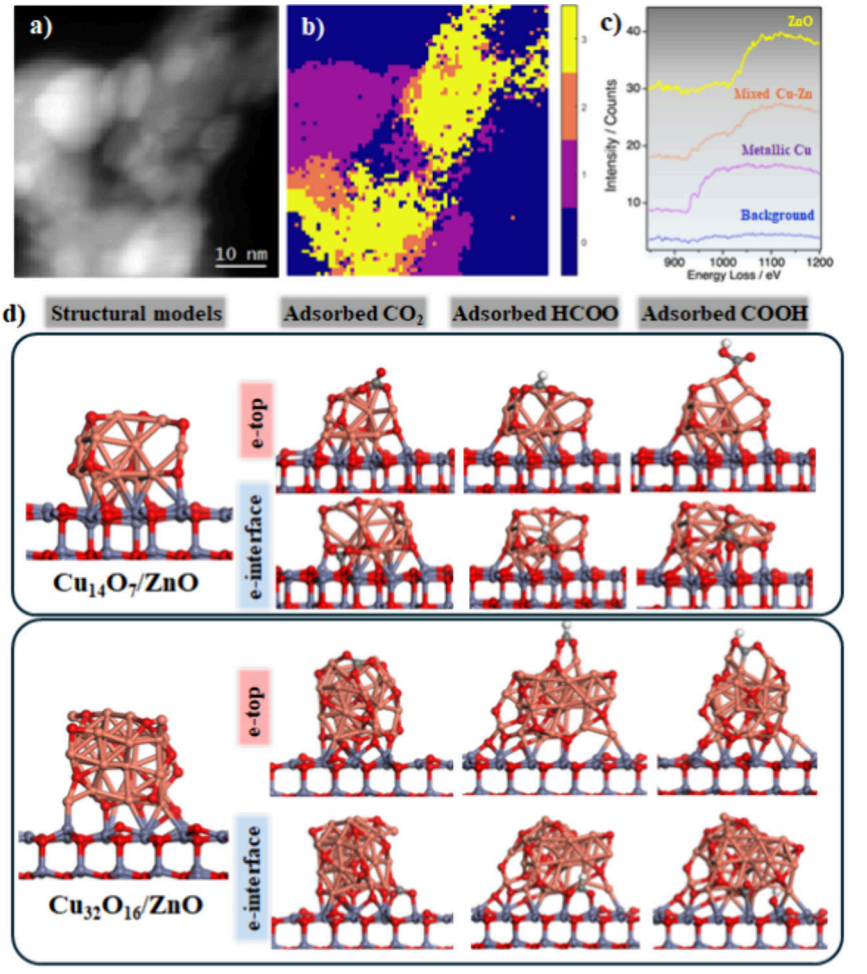
Structure−Activity Correlations

From the results described above, it is demonstrated that in addition to Cu NP (∼15 nm), small copper(I) oxo species in the cluster or even atomic range interacting with ZnO are stabilized in the CuZn-NaOH-0.25 sample. According to the Raman spectra in Figure S19, these entities are also present at higher pressures (i.e., 10 and 20 bar). Notice that this catalyst shows the highest methanol selectivity. In contrast, the coexistence of larger copper(I) oxo species (based on the TPSR-CO analysis) beside Cu NP is observed in the CuZn-NH_4HCO_3 sample, with lower methanol selectivity. The existence of small copper(I) oxo clusters and their involvement in methanol synthesis could explain the unusually low apparent activation energy observed in the CuZn-NaOH-0.25 sample. To rationalize these experimental findings at the molecular level, density functional theory (DFT) calculations were performed to examine the interaction of CO_2 and key intermediates with small copper(I) oxo clusters.

DFT calculations provide additional information highlighting the favorable adsorption of CO_2 over small copper oxo clusters (i.e., $Cu_{14}O_7$ and $Cu_{32}O_{16}$) deposited onto the ZnO (0001) surface (Figure 3d,e and more details in Experimental Methods). In fact, the adsorption energy of CO_2 is much more favorable over $Cu_{14}O_7$ than on other copper(I) oxo configurations, decreasing in the order $Cu_{14}O_7$ (−1.54 eV for e-top and −1.37 eV for e-interface) > $Cu_{32}O_{16}$ (−1.24 eV for e-top and −0.14 eV for e-interface) > Cu_1O_1 (−0.73 eV for e-top) and >> Cu_2O (111) (110) facets (−0.18 and −0.24 eV respectively for e-top) (Figure 3e and Figure S28). Moreover, it is shown that the CO_2 adsorption energy is markedly more favorable on copper oxo clusters than on copper metal, i.e., Cu_{14} (−0.11 eV for e-top and −0.08 eV for e-interface) and Cu_{24} (−0.19 eV for e-top and −0.47eV for e-interface). These results are in line with previous studies,[46] reporting a higher CO_2 interaction with Cu_2O than over metallic copper species. Interestingly, CO_2 binds preferentially on top of the copper oxo clusters, whereas when copper metal species are considered, it binds more favorably at the interface with the support. Additionally, the stabilization of key intermediate species, such as formate and carboxyl species, has been considered and studied by DFT (Figures S29 and S30). Considering carboxyl as an intermediate specie, a systematic evaluation of different adsorption geometries was carried out, including both C−Cu bonding configurations and C−O bonding geometries at the top and interface sites of the different models.

Downloaded from pubs.acs.org/acscacs/article-pdf/16/12/11604/6303569/cs-2026-029073.pdf by CADIZ UNIV user on 22 October 2026

https://doi.org/10.1021/acscatal.6c02907
ACS Catal. 2026, 16, 11604−11617



e) Adsorbed species on the top site (E_{top}) and the cluster ZnO interfacial site (E_{interf})

Systems	CO_2		HCOO		COOH			
	E_{top}, eV	E_{interf}, eV	E_{top}, eV	E_{interf}, eV	E_{top}, eV		E_{interf}, eV	
Cu_{14}/ZnO	-0.11	-0.08	-3.64	-4.93	-1.90		-2.77	
Cu_{24}/ZnO	-0.19	-0.47	-3.24	-3.71	-2.89		-2.12	
					C-Cu	C-O	C-Cu	C-O
$Cu_{14}O_7/ZnO$	-1.54	-1.37	-2.43	-2.64	-2.37	-2.32	-2.63	-3.74
$Cu_{32}O_{16}/ZnO$	-1.24	-0.14	-3.16	-4.51	-3.15	-4.72	-0.42	-4.19
Cu_1O_1/ZnO	-0.73	-	-3.73	-	-2.02	-3.06	-	-
Cu_2O (110)	-0.24	-	-3.09	-	-1.38	-2.03	-	-
Cu_2O (111)	-0.18	-	-2.62	-	-1.23	-2.58	-	-

Figure 3. Elemental STEM-EELS maps for in situ H_2-reduced CuZn-NaOH-0.25 sample. (a) ADF-STEM image acquired while EELS experiment was carried out. (b) The EELS dataset was decomposed by a clustering method, prompting the spatial distribution of the different clusters retrieved. (c) EELS spectra for each cluster. Distribution: background (blue), metallic Cu (purple), mixed CuZn (orange), and ZnO (yellow). (d) DFT-optimized adsorption configurations of CO_2, formate (HCOO), and carboxyl (COOH) species on the top and interface site of $Cu_{14}O_7/ZnO$ and $Cu_{32}O_{16}/ZnO$ models. (e) Calculated adsorption energies of CO_2, formate, and carboxyl species on the top site (E_{top}, eV) of different systems.

The calculated adsorption energies show that carboxyl species can adopt multiple stable configurations. In some cases, C−O bonding configurations provide slightly stronger adsorption than the C−Cu bonding mode. Nevertheless, when all configurations are considered, the overall trend remains unchanged: Carboxyl adsorption is significantly more favorable on small copper(I) oxo clusters, than on metallic Cu clusters or on extended Cu_2O surfaces (Figure 3e and Figure S30).

In agreement with literature,[5,48−52] where the rate-determining step (RDS) in CO_2 hydrogenation to methanol is commonly associated with the hydrogenation of formate or carboxyl intermediates, our results show a good correlation between the stabilization

https://doi.org/10.1021/acscatal.6c02907
ACS Catal. 2026, 16, 11604−11617

Downloaded from pubs.acs.org/acscacs/article-pdf/16/12/11604/6430569/cs-2026-029073.pdf by CADIZ UNIV user on 22 October 2026

energy of the carboxyl species and the observed catalytic activity. However, if formate species are considered as reaction intermediates, then the role of copper(I) oxo clusters is much less evident from the DFT results and does not correlate with the catalytic trends observed experimentally. The above reported correlation supports the hypothesis that carboxyl-type intermediates may play a decisive mechanistic role on Cu(I) oxo sites. However, due to the low optical transmittance of the samples (black, highly absorbing materials), *in situ*/*operando* infrared spectroscopy could not be employed to directly detect surface intermediates. Notably, a recent study[46] proposed a similar mechanism involving carboxyl intermediates over $Cu_{14}O_7$ clusters in the hydrogenation reaction of CO_2 using water as a hydrogen source, in contrast to the conventional formate-mediated pathway observed on metallic Cu nanoparticles. This mechanistic analogy strongly aligns with our theoretical and catalytic observations, supporting the participation of small-size Cu(I) oxo clusters in methanol production, an insight that has been less reported in the literature.[53]

In order to gain a deeper understanding of the catalytic activity of the copper(I) oxo clusters in the CO_2 hydrogenation, supporting the DFT studies, additional experiments have been developed by co-feeding CO in the CO_2 reactant mixture. In particular, time-resolved kinetic studies followed by online mass spectrometry and *in situ* Raman spectroscopic measurements were performed (more details in the Supporting Information). Interestingly, by co-feeding CO, the initial methanol production (i.e., $m/z = 31$) of the CuZn-NaOH-0.25 sample shows a sharp initial increase, followed by a rapid decline to a final value below the starting point (Figure 4a). Note that, after switching back to a CO_2/H_2 feed, the activity returns to the initial value of the catalyst in the presence of only CO_2 (intensity in the methanol signal of 7.2×10^{13}A), pointing to a reversible phenomenon. Moreover, increasing the CO concentration in the reactant feed stresses even more the decay on the final catalytic activity (to an intensity in the methanol signal of 3.2×10^{13} A, Figure 4a). The *in situ* Raman spectroscopic studies carried out under similar reaction conditions (see Figure 4b) show a progressive reduction of the copper(I) oxo clusters in the presence of $CO/CO_2/H_2$, which is complete in the presence of CO/H_2.

The reduction of the Cu(I) oxo species by co-feeding CO is followed by a fast reoxidation after switching back to CO_2/H_2, which entails the recovery of the initial activity observed under this gas mixture. Furthermore, this finding clearly indicates that the copper(I) oxo clusters play a key role in methanol synthesis, where its production increases two-fold upon transition from a reduced to oxidized form. Additional catalytic studies done in a fixed-bed reactor confirm a 1.6-fold increase in methanol production when switching from a $CO/CO_2/H_2$ feed to a CO_2/H_2 one (Table S12). Moreover, it also confirms that the stability of the copper oxo clusters depends on the reactant feed, being stable in CO_2/H_2 but unstable in a $CO/CO_2/H_2$ flow, due to a fast reduction triggered by the presence of CO. The higher methanol signal in the CuZn-NaOH-0.25 sample even after complete reduction of the copper(I) oxo cluster suggests that the interface between copper(I) oxo clusters and the support (Cu (I)-O-Zn (site B in Figure 4c), which remains operative even by co-feeding CO, may play an important role in catalysis. Accordingly, three active sites could be defined in our catalyst, i.e., copper(I) oxo clusters, Cu(I)-O-Zn interface, and Cu nanoparticles or its interaction with the support, labeled as A, B, and C, respectively, in Figure 4c.

This differentiation of active sites is in line with the above reported DFT data, where the sites for CO_2 adsorption in the $Cu_{14}O_7$ cluster follow the order: on top (site A) > at the $Cu_{14}O_7$/ZnO interface (site B) >> at the Cu_{14}/ZnO interface (site C).

Performing similar time-resolved kinetic studies on the CuZn-NH_4HCO_3 sample, which contain larger copper(I) oxo clusters, it is observed, from the *in situ* Raman spectroscopic studies, that the clusters remain stable in a CO/CO_2/He feed, and according to mass data (Figure S31), the methanol production is barely affected by co-feeding CO. The low mass signal of methanol production detected by online mass spectrometry ($\sim 1 \times 10^{13}$ A) evidences a markedly lower reactivity of these sites compared to that of the previous sample, supporting that the higher reactivity of the CuZn-NaOH-0.25 sample arises from the presence of small Cu(I) oxo clusters. Indeed, DFT data show weaker CO_2 adsorption on bigger copper(I) oxo clusters. Moreover, the different redox behaviors of the copper(I) oxo clusters observed in the two samples under CO co-feeding support their different sizes, influencing differently the catalytic performance.

The role of CO in the reactant feed has been controversially discussed in the literature, without a clear trend between different Cu-based samples.[54−60] Some authors[61] report a negative effect of CO at low conversion, whereas it became positive at higher conversion, attributed to water removal by the WGS reaction, shifting the equilibrium of the CO_2 to methanol reaction. Other authors[62] found a promoting effect of CO on Cu/ZnO-based catalysts being strongly affected by the Cu:Zn bulk ratio, whereas their effect on other catalysts such as Cu/Al_2O_3 is markedly lower. This has been vaguely explained by a synergetic effect between Cu and ZnO. According to the results presented in this work, the coexistence of copper(I) oxo clusters of different atomicity, which respond differently under CO flow, could explain part of this controversy, specifically when comparing samples where these entities may or may not be present. In fact, extending our study to other types of Cu-based catalysts usually employed in the literature in the CO_2 hydrogenation to methanol, such as Cu/Al_2O_3, Cu/TiO_2, Cu/MgO, Cu/SiO_2, Cu/Cr_2O_3, Cu/ZnO/Al_2O_3, and Cu/ZrO catalysts, we found marked differences regarding the stabilization of Cu(I)-oxo domains. This can be seen in Figure S20 where the Raman spectra of *in situ* decreased and *operando* samples are displayed. Interestingly, copper oxo clusters are observed on the Cu/ZnO-based catalysts and in the Cu/Cr_2O_3 sample, while absent on the other samples. This can be aligned to the so-called "synergetic effect of ZnO" usually reported in the literature for Cu/ZnO catalysts. Unfortunately, the actual tools do not allow to determine the exact size of those entities as well as their concentration.

Supported by XRD analysis, we propose that the formation of the copper(I) oxo clusters could be related to the stabilization of copper ions in the lattice position of ZnO during the synthesis, which after reduction exsolves with the formation of small copper clusters stabilized on ZnO as demonstrated by STEM-EELS mapping. This is supported in our work from the shift in the XRD peaks associated with ZnO observed in the CuZn-NaOH and CuZn-NH_4OH as-prepared samples (see Figure S2), shifting back after reduction, confirming the exsolution of copper species from lattice positions to extra framework positions. This explains also why the synthesis conditions influence the final size of copper oxo species in the catalyst.

Stability under Reaction Conditions

Finally, the stability of Cu oxo species under long-term operation conditions at 20 bar has been evaluated for the

Downloaded from pubs.acs.org/acscacs/article-pdf/16/12/11604/6430569/cs-2026-029073.pdf by CADIZ UNIV user on 22 October 2026

https://doi.org/10.1021/acscatal.6c02907
ACS Catal. 2026, 16, 11604−11617

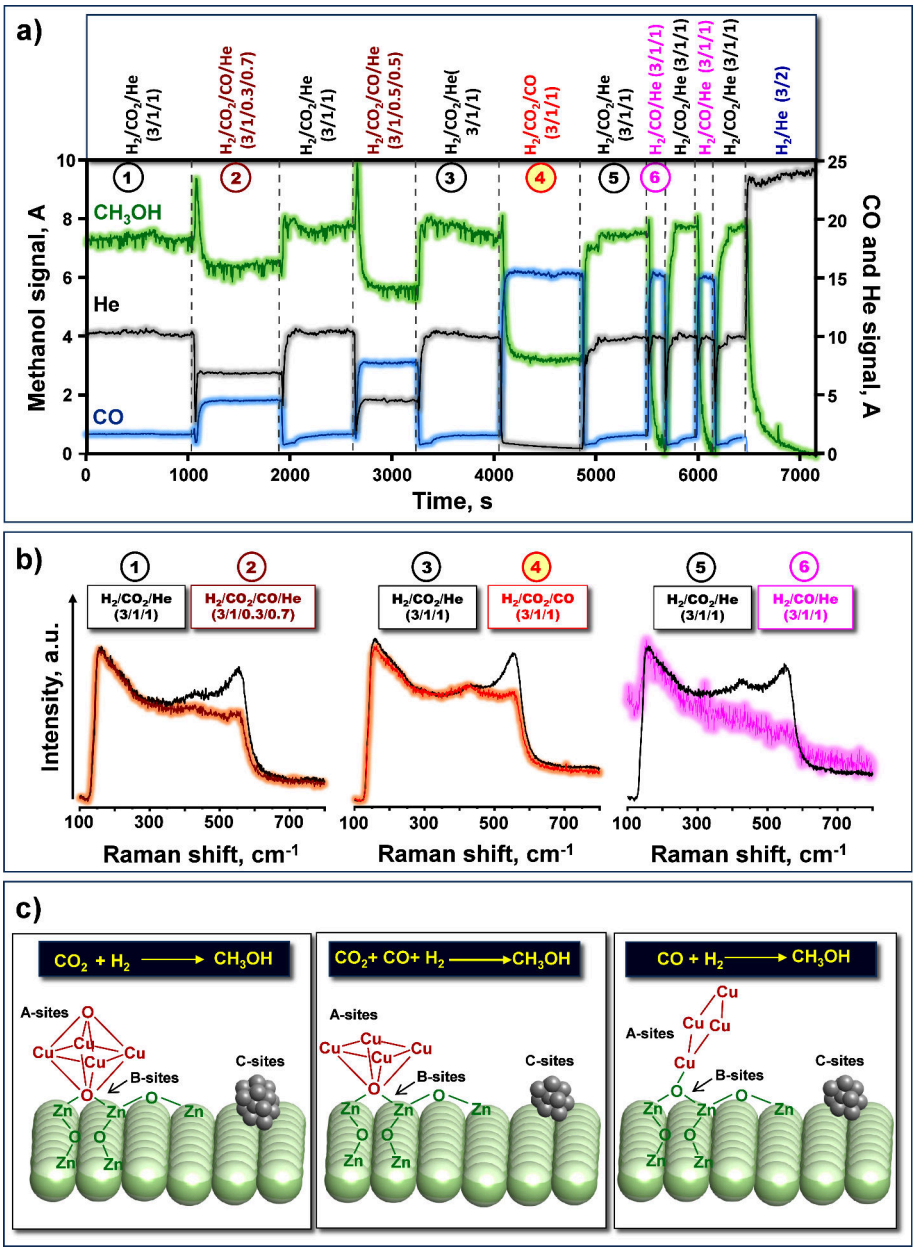


Figure 4. Structure−activity correlation of the different active sites in the CuZn-NaOH-0.25 sample obtained from kinetic and *in situ* Raman studies. (a) MS analysis of methanol production ($m/z = 31$, CH_3OH in 10^{13} A, green line) under alternating feeds of reactants with different compositions. Reaction conditions: 220 °C, 1 bar, 780 mL h^{-1} g_{cat}^{-1}). (b) Raman spectra acquired under similar reaction conditions. (c) Schematic visualization of the participation of different active sites in the catalyst.

CuZn-NaOH-0.25 sample. These Cu(I) oxo clusters remain stable during prolonged reaction conditions (up to 80 h), as confirmed by catalytic stability tests (Table S13 and more details in the Supporting Information, Section 6) together with spectroscopic characterization of the spent catalyst (Figure S35 and Section 6 in the Supporting Information). Meanwhile, sintering of the Cu NP and Zn migration over the Cu NP, with the corresponding loss of H_2 activation capacity, are the main factors responsible for catalyst deactivation. These results point to a synergetic effect between Cu^0 sites for H_2 activation, and small copper(I) oxo clusters in boosting the overall methanol catalytic activity.

To further analyze the stability of the Cu(I) oxo clusters under industrially relevant methanol synthesis conditions, studies at 40 bar have been performed on the CuZn-NaOH-0.25 catalyst in the 220−280 °C temperature range. Catalytic data are included in Table S16 where an increase in methanol production has been observed, consistent with the increase in reaction pressure. On the other hand, the comparable apparent activation energies for methanol and CO formation (Table S17) at 20 and 40 bar suggest the persistence of similar active sites under high-pressure conditions and similar reaction paths. Raman analysis after catalytic tests at 40 bar still revealed the characteristic Cu_2O-like vibrational features associated with highly dispersed small Cu(I)

https://doi.org/10.1021/acscatal.6c02907
ACS Catal. 2026, 16, 11604−11617

Downloaded from pubs.acs.org/acscacs/article-pdf/16/12/11604/6430569/cs-2026-029073.pdf by CADIZ UNIV user on 22 October 2026

oxo clusters (Figure S38). These results demonstrate the structural persistence of the Cu(I) oxo species under elevated-pressure methanol synthesis conditions.

CONCLUSIONS

In conclusion, this work provides atomic-level insights into elusive surface species that are challenging to characterize yet critical for catalytic performance. In this direction, combining *in situ* Raman spectroscopic studies with TPSR-CO and (S)TEM analyses, the presence of small copper(I) oxo clusters in Cu/ZnO-based catalysts, in coexistence with Cu^0, and interacting with the ZnO support has been demonstrated. The critical role of copper(I) oxo clusters in the methanol synthesis has been confirmed by DFT analysis and time-resolved kinetic studies. From DFT studies, it is shown that CO_2 adsorbs preferentially on small $Cu_{14}O_7$ and $Cu_{32}O_{16}$ species than on metallic copper or interfacial sites of the copper metal nanoparticle and the support. Moreover, it has been shown that carboxyl intermediates are preferentially stabilized on small copper oxo clusters versus metallic species, while fewer differences are observed in the stabilization of formate species. The presence of small Cu(I) oxo clusters in the samples involving carboxyl intermediate species could account for the significant low apparent activation energies to methanol production observed in these samples where small copper(I) oxo clusters have been identified. Importantly, the combined experimental evidence demonstrates that these Cu(I) oxo clusters remain present under reaction conditions and are not responsible for catalyst deactivation, which is instead associated with Cu^0 sintering, ZnO surface enrichment, and a reduced H_2 activation capacity.

In a more general way, the results presented in this work not only highlight the structural complexity of a commercial methanol catalyst but also open an interesting research direction in which, contrary to the traditional focus on metallic species and/or its interface with the support, greater attention has to be directed toward the role and behavior of metal oxide species, specifically small metal oxo domains, in relation to their structural, electronic, and catalytic properties.

EXPERIMENTAL METHODS

Catalyst Synthesis

Cu/ZnO-based catalysts (named as CuZn-X−Y) were prepared by a co-precipitation method using different precipitating agents (where X = NH_4HCO_3, NaOH, or NH_4OH) and at different precipitation rates (where Y = 1.0, 0.5, or 0.25 mL min^{-1}). In all cases, a molar chemical composition Cu:Zn of 70:30 was used.

Synthesis of the CuZn-NH_4HCO_3 (Y = 0.5) Catalyst. 8.50 g of $Cu(NO_3)_2{\cdot}3H_2O$ (Sigma-Aldrich, puriss. p.a., 99−104%) and 4.37 g of $Zn(NO_3)_2{\cdot}6H_2O$ (Sigma-Aldrich, reagent grade, 98%) were dissolved in 45.36 g of Milli-Q water. The dissolution of the metal precursors was pumped at 0.5 mL min^{-1} (KD Scientific, KDS-200 syringe pump) into a beaker containing 200 mL of Milli-Q water at 65 °C and under constant stirring (350 rpm). Next, a 1.4 M basic solution of a precipitating agent (NH_4HCO_3, Sigma-Aldrich, 99.5%) was pipetted into the flask in order to keep the pH constant at 6.5. Next, the suspension was aged under stirring at 65 °C for 2 h. The precipitate was then filtered, washed with warm deionized water to pH = 7, and dried overnight at 100 °C to give a blue-green solid. The resulting solid was calcined in a muffle furnace as follows: from 25 to 200 °C (2 °C min^{-1}; dwell time: 1 h), from 200 to 360 °C (2 °C min^{-1}; dwell time: 1 h), and finally held at 360 °C for 9 h. After calcination, a dark solid was obtained.

Synthesis of the CuZn-NaOH-Y (Y = 0.25; 0.5; 1.0) Catalyst. 8.50 g of $Cu(NO_3)_2{\cdot}3H_2O$ (Sigma-Aldrich, puriss. p.a., 99−104%) and 4.37 g of $Zn(NO_3)_2{\cdot}6H_2O$ (Sigma-Aldrich, reagent grade, 98%) were dissolved in 45.36 g of Milli-Q water. The dissolution of the metal precursors was pumped at 0.25, 0.5, and 1.0 mL min^{-1} (KD Scientific, KDS-200 syringe pump) into a beaker containing 200 mL of Milli-Q water at 65 °C and under constant stirring (350 rpm). Next, a 1.4 M basic solution of a precipitating agent (NaOH, Sigma-Aldrich, >98%) was pipetted into the flask in order to keep the pH constant at 6.5. Next, the suspension was aged under stirring at 65 °C for 2 h. The precipitate was then filtered, washed with warm deionized water to pH = 7, and dried overnight at 100 °C to give a dark-brown solid (for 0.25 mL min^{-1}, light brown). The resulting solid was calcined in a muffle furnace as follows: from 25 to 200 °C (2 °C min^{-1}; dwell time: 1 h), from 200 to 360 °C (2 °C min^{-1}; dwell time: 1 h), and finally held at 360 °C for 9 h. After calcination, a dark solid was obtained in all cases.

Synthesis of the CuZn-NH_4OH-Y (Y = 0.25) Catalyst. 8.50 g of $Cu(NO_3)_2{\cdot}3H_2O$ (Sigma-Aldrich, puriss. p.a., 99−104%) and 4.37 g of $Zn(NO_3)_2{\cdot}6H_2O$ (Sigma-Aldrich, reagent grade, 98%) were dissolved in 45.36 g of Milli-Q water. The dissolution of the metal precursors was pumped at 0.25 mL min^{-1} (KD Scientific, KDS-200 syringe pump) into a beaker containing 200 mL of Milli-Q water at 65 °C and under constant stirring (350 rpm). Next, a 1.4 M basic solution of a precipitating agent (NH_4OH, Sigma-Aldrich, 28.0−30.0% NH_3 basis) was pipetted into the flask in order to keep the pH constant at 6.5. Next, the suspension was aged under stirring at 65 °C for 2 h. The precipitate was then filtered, washed with warm deionized water to pH = 7, and dried overnight at 100 °C to give a dark-brown solid. The resulting solid was calcined in a muffle furnace as follows: from 25 to 200 °C (2 °C min^{-1}; dwell time: 1 h), from 200 to 360 °C (2 °C min^{-1}; dwell time: 1 h), and finally held at 360 °C for 9 h. After calcination, a dark solid was obtained.

Catalyst Characterization

The metal contents (Cu and Zn) were analyzed by inductively coupled plasma optical emission spectrometry (ICP-OES) using a Varian 715-ES spectrometer after solid dissolution of the catalysts in an aqueous solution of HNO_3/HCl.

The surface areas of the solid samples (200 mg) were calculated by applying the Brunauer−Emmett−Teller (BET) model to the range of the N_2 adsorption isotherm in which a linear relationship is maintained. The samples were degassed in situ under vacuum at 150 °C. These isotherms were obtained from liquid nitrogen adsorption experiments at −196 °C in a Micromeritics FlowSorb instrument.

X-ray diffraction (XRD) patterns were recorded with a PANalytical Cubix Pro diffractometer using monochromatic Cu Kα radiation (λ = 0.15406 nm). The average sizes of Cu^0 and ZnO crystallites (JCPDS: 01-070-3038 and 01-079-0207, respectively) were calculated from the major peaks (2θ = 50.30 and 56.46, respectively) using the Scherrer equation and assuming a shape factor k = 0.9.

The reducibility of Cu/ZnO-based catalysts was measured by temperature-programmed reduction (TPR-H_2) on a Micromeritics AutoChem 2910. About 50 mg of sample was initially cleaned with 30 mL min^{-1} of Ar at room temperature for 30 min, and then a mixture of 10 vol% of H_2 in Ar was passed through the solid at a total flow rate of 50 mL min^{-1}, while the temperature was increased up to 600 °C at a heating rate of 10 °C min^{-1}. The H_2 consumption was measured using a thermal conductivity detector (TCD).

The amount of copper surface metal sites was measured by surface oxidation with N_2O followed by temperature-programmed reduction with H_2 (TPR-H_2) on a Micromeritics AutoChem 2910 instrument, assuming an adsorption stoichiometry of 1:2 (H_2:Cu_s). Prior to the measurements, 50 mg of the catalysts was activated in a H_2 flow rate of 20 mL min^{-1} (pure H_2, 3 h, 200 °C) for all Cu/ZnO-based samples. After reduction, the samples were cleaned at the same temperature under argon

Downloaded from pubs.acs.org/acscacs/article-pdf/16/12/11604/6430569/cs-2026-029073.pdf by CADIZ UNIV user on 22 October 2026

https://doi.org/10.1021/acscatal.6c02907
ACS Catal. 2026, 16, 11604−11617

flow. The temperature was reduced to 25 °C, and the surface oxidation using N_2O (1 vol% in He, 10 mL min^{-1}) from Cu^0 to Cu_2O was performed for 1 h. After the first treatment, the sample was flushed with argon (15 min) at room temperature. Finally, it was subjected to TPR-H_2 up to 400 °C (10 vol% H_2 in Ar, 50 mL min^{-1}, 10 °C min^{-1}).

Temperature-programmed desorption (TPD-CO_2) studies over *in situ* reduced samples were performed using a ChemStar TPx (chemisorption analyzer) instrument with a quartz reactor at atmospheric pressure, connected online to a mass spectrometer (MS) OMNISTAR (GSD 320 Gas Analysis System) and a thermal conductivity detector (TCD). First, samples (ca. 50 mg diluted in 300 mg of SiC) were activated at 200 °C in a pure H_2 flow rate of 20 mL min^{-1} for 3 h. Then, the sample was cleaned with Ar (20 mL min^{-1}) at room temperature for 30 min. After stabilization, CO_2 was pulsed to the sample 20 times using a four-way valve (61.0 μL loop) at 50 mL min^{-1} (5% CO_2 in Ar) for 1 h. After the adsorption step, physisorbed CO_2 was eliminated by using an Ar steam (50 mL min^{-1}) for 30 min. After that, chemisorbed CO_2 desorption measures took place at increasing temperatures (from room temperature up to 600 °C), keeping the inert flow rate at 50 mL min^{-1}. The CO_2 desorption was followed by MS ($m/z = 44$).

Surface studies by X-ray photoelectron spectroscopy (XPS) at the laboratory scale were recorded with a SPECS spectrometer equipped with a Phoibos 150 MCD-9 multichannel analyzer using a non-monochromatic AlKα (1486.6 eV) X-ray source. The spectra were recorded with an X-ray power of 50 W, a pass energy of 30 eV, and an operating pressure of 10^{-9} mbar. The sample (≈10−30 mg) was pressed into a pellet and loaded onto a SPECS stainless-steel sample holder. Before XPS analysis, Cu/ZnO samples were submitted to different treatments in a high-pressure reactor (HPCR) connected under UHV to the XPS analysis chamber: (i) calcined at 360 °C; (ii) in situ reduction (25 mL min^{-1} H_2 flow rate) at 200 °C and at atmospheric pressure for 3 h; (iii) in situ CO_2 hydrogenation to methanol at 260 °C (≈2 h), 10 bar pressure in a CO_2:H_2 mixture (1:3 molar ratio, 20 mL min^{-1} total flow rate). Gases were flown through two mass flow controllers (Bronkhorst). XPS spectra were referenced to the Zn 2p peak (1022.0 eV), and data treatment was addressed using CASA XPS software.

Raman spectroscopy studies were performed using a Renishaw "in Via" spectrometer connected to an Olympus microscope. The instrument is equipped with a He−Ne green laser (514 nm), a diode laser (785 nm), and a CCD detector. *In situ* Raman studies at 1 bar were performed with a Linkam THMS600 cell, which allows working in a temperature range from −195 to 600 °C and with precision and stability of 0.01 °C, whereas in studies at different pressures, a high-pressure and high-temperature Harrick cell was used equipped with a backpressure regulator (BPR, Swagelok) that allows working in the pressure range of 1−20 bar and a temperature controller that allows working in the range of 25 to 1250 °C.

Typically, for *in situ* Raman studies at 1 bar, samples are reduced *ex situ* in H_2 (20 mL min^{-1}) and exposed to air for 1 h. Then, they are reduced in situ in H_2 (20 mL min^{-1}) to 200 °C and brought down to room temperature under the same conditions. Then, the temperature is increased to 280 °C in inert Ar atmosphere (20 mL min^{-1}); after about 15 min, the temperature is lowered to 260 °C; and finally, the samples are exposed to reaction conditions, i.e., CO_2/H_2=1/3 (20 mL min^{-1}) and in the temperature range of 260−280 °C. On the other hand, the studies at different pressures followed a similar procedure but without the inert atmosphere treatment, i.e., after *in situ* reduction in H_2 (20 mL min^{-1}), the temperature is increased in the range of 260−280 °C in H_2 and switched to reaction conditions by feeding CO_2/H_2 at the pressures of 1, 10, and 20 bar. Finally, *in situ* Raman studies were also performed by co-feeding different proportions of CO to the reactant feed.

Advanced electron microscopy studies were performed in a double-corrected FEI Titan Cubed Themis 60-300, operated at 200 kV (Cs = 0.001 mm and sub-angstrom resolution). The microscope is equipped with a Super X-G2 detector and coupled to a GIF Continuum EELS spectrometer that allow to conduct high-quality X-ray energy-dispersive spectroscopy (XEDS) and electron energy-loss spectroscopy (EELS). To accomplish the *ex situ* measurements, the sample of interest was loaded on a holey carbon-coated Au grid. Images were recorded in either high-resolution TEM (HRTEM) or high-angle annular dark-field STEM (HAADF-STEM) imaging modes. The XEDS maps tracked the Cu-K (8.0 keV) and Zn-K (8.6 keV) lines, using a beam current of ∼100 pA and a dwell time of 150 μs. A Gaussian-blur post-processing filtering ($s = 0.8$) was applied for enhancing visualization. In the case of EELS, the Cu-$L_{2,3}$ and Zn-$L_{2,3}$ edges were monitored (930−950 and 1020−1040 eV, respectively). The beam current was set to ∼30 pA to avoid beam-induced modifications, with an energy dispersion of 0.25 eV/channel, a pixel time of 0.2 s, and a camera length of 29.5 mm that provides a collection angle of 50−70 mrad. The fine-structure details of the Cu-$L_{2,3}$ edge (Energy-Loss Near Edge Structure or ELNES) was used to monitor the oxidation state of this element. HRTEM imaging of *ex situ* samples was also performed using a FEI Titan Cubed image-corrected microscope at 300 kV. The *ex situ* reduced samples were drop-casted on holey carbon-coated Cu grids. These TEM grids were annealed at 200 °C under a H_2 flow for 3 h. The grids were exposed to air less than 5 min before being loaded into the microscope.

For *in situ* STEM, a DENSsolutions Climate+ gas flow and heating holder was used. In this case, 0.5 mL of a dispersion containing 0.25 mg of the previously reduced catalyst powder in 1 mL of isopropanol was deposited on a silicon nitride chip and further dried under air. To remove solvent remnants, the sample was first heated from room temperature up to 200 °C under flowing nitrogen (0.1 mL min^{-1}) at nearly atmospheric pressure (910 mbar). Treatment was prolonged for 1 h after reaching the highest temperature. After cleaning, the gas flow was switched, at 200 °C, to 50% H_2/50% N_2, flowing under the same conditions. EELS characterization was performed under flowing the reducing mixture. After this, pure N_2 was used to flush the nanoreactor and remove the reducing gas. Finally, a flow of 50% O_2/50% N_2 was introduced into the reactor to study the sample under an oxidizing atmosphere, keeping the same reaction conditions (200 °C, 910 mbar).

Temperature-programmed surface reaction CO (TPSR-CO) studies over *in situ* reduced samples were performed in a quartz reactor at atmospheric pressure, connected online to a mass spectrometer (MS) Balzer (QMG 220 M1). First, 150 mg of sample diluted in 250 mg of SiC was activated at 200 °C, in 20 mL min^{-1} of H_2 and for 3 h. Then, the sample was cleaned in Ar (20 mL min^{-1}) at room temperature for 30 min. After this step, a CO flow (20 mL min^{-1} of 4% CO and the rest He) was passed through the sample at 25 °C for 1 h, followed by increasing the temperature from 25 to 500 °C with a ramp of 10 °C min^{-1}. The gas effluent was followed by MS ($m/z = 1$ (H_2); 4 (He); 28 (CO); and 44 (CO_2)). On the other hand, temperature-programmed surface reaction CO (TPSR-CO) studies on *in situ* reduced samples followed by exposure to controlled pulses of O_2 have also been performed, in order to follow the degree of copper oxidation and correlate with *in situ* HRTEM studies. Concretely, the same procedure as above is followed, where two to three pulses of pure O_2 (100 μL) were added to the sample with a four-way valve after the reduction and clean-up steps in Ar at room temperature.

Kinetic studies under alternating feed compositions were carried out on a home-built reaction system composed of two gas lines and a four-way valve connected to a low dead volume reactor (hold-up in the gas phase <20 s) to guarantee adequate temporal resolution. The effluent was continuously monitored in a mass spectrometer (MS) following the signals, m/z, 4 (He), 28 (CO + N_2), 31 (CH_3OH), and 44 (CO_2). Samples were activated in situ at 200 °C for 3 h in a H_2 gas flow of 20 mL min^{-1}. Two reaction mixtures were used: (i) CO-free feed (H_2/CO_2/He = 3/1/1) and (ii) a CO-containing feed with different CO concentrations ($H_2/CO_2/CO$/He = 3/1/0.3/0.7; 3/1/0.5/0.5; 3/1/1/0; or 3/0/1/1). The feeds were switched alternatively with the help of the four-way valve. The study was done under steady-state reaction conditions operating at 220 °C, 1 bar, and a total gas flow of 50 mL min^{-1}.

Computational Details

All density functional theory (DFT) calculations were performed using the Vienna Ab initio Simulation Package (VASP).[63,64] The projector

Downloaded from pubs.acs.org/acscacs/article-pdf/16/12/11604/6430569/cs-2026-029073.pdf by CADIZ UNIV user on 22 October 2026

https://doi.org/10.1021/acscatal.6c02907
ACS Catal. 2026, 16, 11604−11617

augmented wave (PAW) method was adopted together with the revised Perdew–Burke–Ernzerhof (PBE) exchange-correlation functional.[65,66] A plane-wave cutoff energy of 400 eV was applied. Copper metal and oxo clusters including Cu_{14}, Cu_{24}, $Cu_{14}O_7$, $Cu_{32}O_{16}$, and Cu_1O_1 were first optimized in a cubic box of 20 × 20 × 20 Å, with the Brillouin zone sampled by a 3 × 3 × 3 Monkhorst–Pack *k*-point mesh. The ZnO (0001) surface was modeled using a 6 × 6 surface supercell composed of six atomic layers. A vacuum region of 20 Å was introduced along the surface normal to avoid interactions between periodic images. The optimized copper metal and oxo clusters were then deposited onto the ZnO (0001) surface, resulting in supported configurations Cu_{14}/ZnO, Cu_{24}/ZnO, $Cu_{14}O_7$/ZnO, $Cu_{32}O_{16}$/ZnO, and Cu_1O_1/ZnO. In addition, slab models of Cu_2O (110) and Cu_2O (111) surfaces were generated. Both surfaces were constructed using 2 × 2 surface supercells with four atomic layers, separated by a vacuum region of 15 Å. The purpose of constructing these models was to systematically cover a broad range of active species with different sizes. In particular, Cu_1O_1/ZnO and the extended Cu_2O surfaces represent two extremes of oxo clusters, corresponding to the smallest and the largest limits, respectively. During the structural optimizations, the bottom two atomic layers of the ZnO (0001) slab were fixed at their bulk positions, while all other atoms were allowed to relax.

We evaluated the adsorption energies (E_{ads}) of CO_2, formate, and carboxyl species on two classes of sites: (i) the top site of oxo clusters and metallic copper and (ii) the cluster-ZnO interfacial region. For each adsorbate (A) and site (S), the E_{ads} was computed in the same supercell using a far-field reference to cancel spurious box-size effects:

$$E_{ads} = E_{final}(A@S) - E_{initial}(A_{far} + S) \quad (1)$$

where $E_{final}(A@S)$ is the total energy after fully relaxing the geometry with A adsorbed at site S. $E_{initial}(A_{far} + S)$ is the total energy of the same slab/cluster configuration with the adsorbate placed far from any surface or cluster atom (i.e., in the vacuum region, separated by >10 Å from the nearest atom) so that it does not interact with the substrate. Both calculations use identical cells, *k*-point meshes, and numerical settings.

Catalyst Evaluation

Catalytic studies of CO_2 hydrogenation to methanol were performed in a stainless-steel fixed-bed reactor (11 mm inner diameter and 240 mm length), equipped with a backpressure regulator (BPR, Swagelok) that allows working at a pressure range of 1–40 bar. Typically, 200 mg of catalyst (particle size 400–600 mm) was diluted in SiC at a weight ratio of 0.12 (Cat/SiC). Samples were reduced in situ at atmospheric pressure prior to catalytic tests (20 mL min^{-1} of H_2, 200 °C, 10 °C min^{-1} and 3 h). Constant weight hourly space velocity experiments (WHSV, 30,000 mL h^{-1} g_{cat}^{-1}) were performed under concentrated reaction conditions (i.e., 23.7 vol % CO_2, 71.3 vol % H_2, and 5.0 vol % N_2) and pressure of 40, 20, or 1 bar. Reaction temperatures ranged from 180 to 280 °C. In addition, catalytic experiments were carried out at varying WHSV (120,000–3846.2 mL h^{-1} g_{cat}^{-1}) at a constant molar ratio of $H_2/CO_2 = 3$ and pressure of 20 or 1 bar. Online gas chromatography (GC) using Agilent-8860 equipment with TCD (PLOT/U + mol sieve column) and FID (BR-Q Plot column) detectors performed direct analysis of the reaction products. Blank experiments (in the presence of SiC) showed the absence of a homogeneous contribution to the reaction.

■ ASSOCIATED CONTENT

Data Availability Statement

The data that support the findings of this study are available in the supplementary material of this article.

Supporting Information

The Supporting Information is available free of charge at https://pubs.acs.org/doi/10.1021/acscatal.6c02907.

Physicochemical characterization of the catalysts, including XRD, XPS, Raman spectroscopy, HRTEM, STEM-EELS, TPSR-CO, CO_2-TPD, and H_2-D_2 exchange analyses; catalytic performance data at different temperatures, space velocities, contact times, and reaction pressures (1, 10, 20, and 40 bar); apparent activation energies together with initial CO and methanol formation rates; transient kinetic studies under CO co-feeding conditions followed by online mass spectrometry and operando Raman spectroscopy; long-term catalytic stability studies and post-reaction characterization; DFT optimized adsorption configurations and adsorption energy calculations for CO_2, HCOO, and COOH intermediates on different Cu-based models; and comparative literature tables related to Cu-based catalysts and Cu(I) oxo species in methanol synthesis and other catalytic reactions (DOCX)

■ AUTHOR INFORMATION

Corresponding Author

P. Concepción – *Instituto de Tecnología Química, Consejo Superior de Investigaciones Científicas, Universitat Politècnica de València (CSIC-UPV), Avenida de los Naranjos s/n, Valencia 46022, Spain;* orcid.org/0000-0003-2058-3103; Email: pconcepc@upvnet.upv.es

Authors

J. Soriano – *Instituto de Tecnología Química, Consejo Superior de Investigaciones Científicas, Universitat Politècnica de València (CSIC-UPV), Avenida de los Naranjos s/n, Valencia 46022, Spain;* orcid.org/0000-0002-8965-0063

Y. Fo – *State Key Laboratory of Heavy Oil Processing, China University of Petroleum (Beijing), Beijing 102249, China*

D. Gómez – *Instituto de Tecnología Química, Consejo Superior de Investigaciones Científicas, Universitat Politècnica de València (CSIC-UPV), Avenida de los Naranjos s/n, Valencia 46022, Spain;* orcid.org/0000-0003-0010-4507

J.M. López Nieto – *Instituto de Tecnología Química, Consejo Superior de Investigaciones Científicas, Universitat Politècnica de València (CSIC-UPV), Avenida de los Naranjos s/n, Valencia 46022, Spain*

A. Roy – *Instituto de Nanociencia y Materiales de Aragón (INMA), CSIC-Universidad de Zaragoza, Zaragoza 50009, Spain; Laboratorio de Microscopías Avanzadas (LMA), Universidad de Zaragoza, Zaragoza 50018, Spain;* orcid.org/0000-0001-8483-8609

R. Manzorro – *Departamento de Ciencia de los Materiales e Ingeniería Metalúrgica y Química Inorgánica, Facultad Ciencias, Universidad de Cádiz, Campus Rio San Pedro. Puerto Real, Cádiz 11510, Spain;* orcid.org/0000-0002-4510-7106

R. Arenal – *Instituto de Nanociencia y Materiales de Aragón (INMA), CSIC-Universidad de Zaragoza, Zaragoza 50009, Spain; Laboratorio de Microscopías Avanzadas (LMA), Universidad de Zaragoza, Zaragoza 50018, Spain; ARAID Foundation, Zaragoza 50018, Spain;* orcid.org/0000-0002-2071-9093

J.J. Calvino – *Departamento de Ciencia de los Materiales e Ingeniería Metalúrgica y Química Inorgánica, Facultad Ciencias, Universidad de Cádiz, Campus*

Downloaded from pubs.acs.org/acscacs/article-pdf/16/12/11604/6430569/cs-2026-029073.pdf by CADIZ UNIV user on 22 October 2026

https://doi.org/10.1021/acscatal.6c02907
ACS Catal. 2026, 16, 11604–11617

Rio San Pedro. Puerto Real, Cádiz 11510, Spain;
orcid.org/0000-0002-0989-1335
W. Song – *State Key Laboratory of Heavy Oil Processing, China University of Petroleum (Beijing), Beijing 102249, China;*
orcid.org/0000-0001-5720-204X

Complete contact information is available at:
https://pubs.acs.org/doi/10.1021/acscatal.6c02907

Author Contributions

‡J.S and Y.F. contributed equally to this work. Conceptualization: J.M.L.N., J.J.C., and P.C. Methodology: J.S., D.G., J.M.L.N., A.R., R.A., R.M., J.J.C., P.C., Y.F., and W.S. Investigation: J.S., D.G., J.M.L.N., A.R., R.A., R.M., J.J.C., P.C., Y.F., and W.S. Visualization: J.S., D.G., J.M.L.N., A.R., R.A., R.M., J.J.C., P.C., and W.S. Funding acquisition: J.M.L.N. and P.C. Project administration: J.M.L.N. and P.C. Supervision: J.M.L.N. and P.C. Writing—original draft: J.J.C. and P.C. Writing—review and editing: J.S., D.G., J.M.L.N., A.R., R.A., R.M., J.J.C., P.C., and W.S.

Notes

The authors declare no competing financial interest.

■ ACKNOWLEDGMENTS

This research was funded by Ministerio de Ciencia, Innovación y Universidades, grant numbers PID2021-1262350B-C31, PID2020-113006-RB-I00, and PID2023-151080NB-I00; CEX2023-001286-S funded by MCIN/AEI/10.13039/501100011033; and the Government of Aragon (DGA) through the project E13_23R and Generalitat Valenciana (GVA), grant number CIAICO/2021/2138. This study forms part of the Advanced Materials program and was supported by MCIN with funding from European Union Next Generation EU (PRTR-C17.11) and Generalitat Valenciana (TED2021-130756B-C32and ref MFA/2022/016). Financial support by the Spanish Ministry of Science and Innovation (CEX2021-001230-S grant funded by MCIN/AEI/10.13039/501100011033) is gratefully acknowledged. D.G. thanks the Marie-Curie Postdoctoral (MSCA) Fellowship ID 101154019.

■ REFERENCES

(1) Zhao, D.; Ortner, N.; Holena, M.; Wohlrab, S.; Kondratenko, E. V. Identifying Catalyst Property Descriptors for CO_2 Hydrogenation to Methanol via Big-Data Analysis. *ACS Catal.* **2023**, *13* (16), 10547–10559.

(2) Suvarna, M.; Araújo, T. P.; Pérez-Ramírez, J. A Generalized Machine Learning Framework to Predict the Space-Time Yield of Methanol from Thermocatalytic CO_2 Hydrogenation. *Appl. Catal., B* **2022**, *315*, No. 121530.

(3) Senanayake, S. D.; Ramírez, P. J.; Waluyo, I.; Kundu, S.; Mudiyanselage, K.; Liu, Z.; Liu, Z.; Axnanda, S.; Stacchiola, D. J.; Evans, J.; Rodriguez, J. A. Hydrogenation of CO_2 to Methanol on CeO_x/Cu(111) and ZnO/Cu(111) Catalysts: Role of the Metal-Oxide Interface and Importance of Ce^{3+} Sites. *J. Phys. Chem. C* **2016**, *120* (3), 1778–1784.

(4) Beck, A.; Newton, M. A.; van de Water, L. G. A.; van Bokhoven, J. A. The Enigma of Methanol Synthesis by Cu/ZnO/Al_2O_3-Based Catalysts. *Chem. Rev.* **2024**, *124* (8), 4543–4678.

(5) Kattel, S.; Ramírez, P. J.; Chen, J. G.; Rodriguez, J. A.; Liu, P. Active Sites for CO_2 Hydrogenation to Methanol on Cu/ZnO Catalysts. *Science* **2017**, *355* (6331), 1296–1299.

(6) Kuld, S.; Conradsen, C.; Moses, P. G.; Chorkendorff, I.; Sehested, J. Quantification of Zinc Atoms in a Surface Alloy on Copper in an Industrial-Type Methanol Synthesis Catalyst. *Angew. Chem., Int. Ed.* **2014**, *53* (23), 5941–5945.

(7) Li, M. M. J.; Zeng, Z.; Liao, F.; Hong, X.; Tsang, S. C. E. Enhanced CO_2 Hydrogenation to Methanol over CuZn Nanoalloy in Ga Modified Cu/ZnO Catalysts. *J. Catal.* **2016**, *343*, 157–167.

(8) Behrens, M.; Studt, F.; Kasatkin, I.; Kühl, S.; Hävecker, M.; Abild-Pedersen, F.; Zander, S.; Girgsdies, F.; Kurr, P.; Kniep, B.-L.; Tovar, M.; Fischer, R. W.; Nørskov, J. K.; Schlögl, R. The Active Site of Methanol Synthesis over Cu/ZnO/Al_2O_3 Industrial Catalysts. *Science* **2012**, *336* (6083), 893–897.

(9) Lunkenbein, T.; Schumann, J.; Behrens, M.; Schlögl, R.; Willinger, M. G. Formation of a ZnO Overlayer in Industrial Cu/ZnO/Al_2O_3 Catalysts Induced by Strong Metal–Support Interactions. *Angew. Chem., Int. Ed.* **2015**, *127* (15), 4627–4631.

(10) Divins, N. J.; Kordus, D.; Timoshenko, J.; Sinev, I.; Zegkinoglou, I.; Bergmann, A.; Chee, S. W.; Widrinna, S.; Karslıoğlu, O.; Mistry, H.; Luna, M. L.; Zhong, J. Q.; Hoffman, A. S.; Boubnov, A.; Boscoboinik, J. A.; Heggen, M.; Dunin-Borkowski, R. E.; Bare, S. R.; Roldan Cuenya, B. Operando high-pressure investigation of size-controlled CuZn catalysts for the methanol synthesis reaction. *Nat. Commun.* **2021**, *12*, No. 1435.

(11) Wu, C.; Lin, L.; Liu, J.; Zhang, J.; Zhang, F.; Zhou, T.; Rui, N.; Yao, S.; Deng, Y.; Yang, F.; Xu, W.; Luo, J.; Zhao, Y.; Yan, B.; Wen, X-D.; Rodriguez, J. A.; Ma, D. Inverse ZrO_2/Cu as a highly efficient methanol synthesis catalyst from CO_2 hydrogenation. *Nat. Commun.* **2020**, *11*, No. 5767.

(12) Shi, P.; Han, J.; Tian, Y.; Wang, J.; Lv, Y.; Li, Y.; Zhang, X.; Li, C. Engineering CuZnOAl_2O_3 Catalyst for Enhancing CO_2 Hydrogenation to Methanol. *Molecules* **2025**, *30*, No. 1350.

(13) Cored, J.; Mazarío, J.; Cerdá-Moreno, C.; Lustemberg, P. G.; Ganduglia-Pirovano, M. V.; Domine, M. E.; Concepción, P. Enhanced Methanol Production over Non-Promoted Cu-MgO-Al_2O_3 Materials with Ex-Solved 2 Nm Cu Particles: Insights from an Operando Spectroscopic Study. *ACS Catal.* **2022**, *12* (7), 3845–3857.

(14) Han, A.; Ding, J.; Zhong, Q. Role of single-atom Pd in Cu/ZrO_2 catalysts for CO_2 hydrogenation to methanol. *Colloids Surf., A* **2022**, *641*, No. 128535.

(15) Liu, X.; Wang, H.; Lu, J. Recent Progress in Understanding the Nature of Active Sites for Methanol Synthesis over Cu/ZnO Catalysts. *J. Catal.* **2024**, *436*, No. 115561.

(16) Ling, L-L.; Guan, X.; Liu, X.; Lei, X-M.; Lin, Z.; Jiang, H-L. Promoted hydrogenation of CO_2 to methanol over single-atom Cu sites with Na^+-decorated microenvironment. *Natl. Sci. Rev.* **2024**, *11* (6), No. nwae114.

(17) Comas-Vives, A.; Copéret, C. Nature and Dynamics of Active Sites in Cu-Based Catalysts for the CO_2 Hydrogenation to Methanol. *Acc. Chem. Res.* **2026**, *59* (1), 27–39.

(18) Xu, Y.; Wang, M.; Xie, Z.; Tian, D.; Sheng, G.; Tang, X.; Li, H.; Wu, Y.; Song, C.; Gao, X.; Yao, S.; Ma, D.; Lin, L. Insights into the interfacial structure of Cu/ZrO_2 catalysts for methanol synthesis from CO_2 hydrogenation: Effects of Cu-supported nano-ZrO_2 inverse interface. *Chem. Eng. J.* **2023**, *470*, No. 144006.

(19) Wu, W.; Wang, Y.; Luo, L.; Wang, M.; Li, Z.; Chen, Y.; Wang, Z.; Chai, J.; Cen, Z.; Shi, Y.; Zhao, J.; Zeng, J.; Li, H. CO_2 Hydrogenation over Copper/ZnO Single-Atom Catalysts: Water-Promoted Transient Synthesis of Methanol. *Angew. Chem., Int. Ed.* **2022**, *61* (48), No. e202213024.

(20) Zhao, H.; Yu, R.; Ma, S.; Xu, K.; Chen, Y.; Jiang, K.; Fang, Y.; Zhu, C.; Liu, X.; Tang, Y.; Wu, L.; Wu, Y.; Jiang, Q.; He, P.; Liu, Z.; Tan, L. The Role of Cu_1–O_3 Species in Single-Atom Cu/ZrO_2 Catalyst for CO_2 Hydrogenation. *Nat. Catal.* **2022**, *5* (9), 818–831.

(21) Xu, D.; Hong, X.; Liu, G. Highly Dispersed Metal Doping to ZnZr Oxide Catalyst for CO_2 Hydrogenation to Methanol: Insight into Hydrogen Spillover. *J. Catal.* **2021**, *393*, 207–214.

(22) Chen, A.; Yu, X.; Zhou, Y.; Miao, S.; Li, Y.; Kuld, S.; Sehested, J.; Liu, J.; Aoki, T.; Hong, S.; Camellone, M. F.; Fabris, S.; Ning, J.; Jin, C.; Yang, C.; Nefedov, A.; Wöll, C.; Wang, Y.; Shen, W. Structure of the

Downloaded from pubs.acs.org/acscacs/article-pdf/16/12/11604/6430569/cs-2026-029073.pdf by CADIZ UNIV user on 22 October 2026

Catalytically Active Copper–Ceria Interfacial Perimeter. *Nat. Catal.* **2019**, *2* (4), 334–341.
(23) Liu, H. X.; Li, S. Q.; Wang, W. W.; Yu, W. Z.; Zhang, W. J.; Ma, C.; Jia, C. J. Partially Sintered Copper–ceria as Excellent Catalyst for the High-Temperature Reverse Water Gas Shift Reaction. *Nat. Commun.* **2022**, *13* (1), No. 867.
(24) Jin, S.; Kwon, C.; Bugaev, A.; Karakurt, B.; Lin, Y. C.; Savereide, L.; Zhong, L.; Boureau, V.; Safonova, O.; Kim, S.; Luterbacher, J. S. Atom-by-Atom Design of Cu/ZrO_x Clusters on MgO for CO_2 Hydrogenation Using Liquid-Phase Atomic Layer Deposition. *Nat. Catal.* **2024**, *7* (11), 1199–1212.
(25) Yang, B.; Liu, C.; Halder, A.; Tyo, E. C.; Martinson, A. B. F.; Seifert, S.; Zapol, P.; Curtiss, L. A.; Vajda, S. Copper Cluster Size Effect in Methanol Synthesis from CO_2. *J. Phys. Chem. C* **2017**, *121* (19), 10406–10412.
(26) Zhong, J.; Yang, X.; Wu, Z.; Liang, B.; Huang, Y.; Zhang, T. State of the Art and Perspectives in Heterogeneous Catalysis of CO_2 Hydrogenation to Methanol. *Chem. Soc. Rev.* **2020**, *49* (5), 1385–1413.
(27) Van Den Berg, R.; Prieto, G.; Korpershoek, G.; Van Der Wal, L. I.; Van Bunningen, A. J.; Lægsgaard-Jørgensen, S.; De Jongh, P. E.; De Jong, K. P. Structure Sensitivity of Cu and CuZn Catalysts Relevant to Industrial Methanol Synthesis. *Nat. Commun.* **2016**, *7*, No. 13057.
(28) Ullah Awan, S.; Hasanain, S. K.; Bertino, M. F.; Hassnain Jaffari, G. Ferromagnetism in Li Doped ZnO Nanoparticles: The Role of Interstitial Li. *J. Appl. Phys.* **2012**, *112* (10), No. 103924-103924-9.
(29) Fernández-Villanueva, E.; Lustemberg, P. G.; Zhao, M.; Soriano Rodriguez, J.; Concepción, P.; Ganduglia-Pirovano, M. V. Water and Cu^+ Synergy in Selective CO_2 Hydrogenation to Methanol over $Cu\text{-}MgO\text{-}Al_2O_3$ Catalysts. *J. Am. Chem. Soc.* **2024**, *146* (3), 2024–2032.
(30) Pacchioni, G. From CO_2 to Methanol on $Cu/ZnO/Al_2O_3$ Industrial Catalyst. What Do We Know about the Active Phase and the Reaction Mechanism? *ACS Catal.* **2024**, *14* (4), 2730–2745.
(31) Cored, J.; Lopes, C. W.; Liu, L.; Soriano, J.; Agostini, G.; Solsona, B.; Sánchez-Tovar, R.; Concepción, P. $Cu\text{-}Ga^{3+}$-Doped Wurtzite ZnO Interface as Driving Force for Enhanced Methanol Production in Co-Precipitated $Cu/ZnO/Ga_2O_3$ Catalysts. *J. Catal.* **2022**, *407*, 149–161.
(32) Gómez, D.; Collins, S.; Concepción, P.; Jiménez, R.; Karelovic, A. Elucidating the Promotional Effect of Ultra-Low Zn Content on Cu for CO_2 Hydrogenation to Methanol. *J. Catal.* **2023**, *427*, No. 115119.
(33) Karelovic, A.; Ruiz, P. The Role of Copper Particle Size in Low Pressure Methanol Synthesis via CO_2 Hydrogenation over Cu/ZnO Catalysts. *Catal. Sci. Technol.* **2015**, *5* (2), 869–881.
(34) Zhao, F.; Fan, L.; Xu, K.; Hua, D.; Zhan, G.; Zhou, S. F. Hierarchical Sheet-like Cu/Zn/Al Nanocatalysts Derived from LDH/MOF Composites for CO_2 Hydrogenation to Methanol. *J CO2 Util.* **2019**, *33*, 222–232.
(35) Choi, Y.; Futagami, K.; Fujitani, T.; Nakamura, J. The Role of ZnO in Cu/ZnO Methanol Synthesis Catalysts-Morphology Effect or Active Site Model? **2001**, *208*, 163–167.
(36) Steimecke, M.; Araújo-Cordero, A. M.; Dieterich, E.; Bron, M. Probing Individual Cuprous Oxide Microcrystals towards Carbon Dioxide Reduction by Using In Situ Raman-Coupled Scanning Electrochemical Microscopy. *ChemElectroChem* **2022**, *9* (3), No. e202101221.
(37) Niaura, G. Surface-Enhanced Raman Spectroscopic Observation of Two Kinds of Adsorbed OH^- Ions at Copper Electrode. *Electrochim. Acta* **2000**, *45* (21), 3507–3519.
(38) Bodappa, N.; Su, M.; Zhao, Y.; Le, J. B.; Yang, W. M.; Radjenovic, P.; Dong, J. C.; Cheng, J.; Tian, Z. Q.; Li, J. F. Early Stages of Electrochemical Oxidation of Cu(111) and Polycrystalline Cu Surfaces Revealed by in Situ Raman Spectroscopy. *J. Am. Chem. Soc.* **2019**, *141* (31), 12192–12196.
(39) Sun, Y.; Huang, C.; Chen, L.; Zhang, Y.; Fu, M.; Wu, J.; Ye, D. Active Site Structure Study of Cu/Plate ZnO Model Catalysts for CO_2 Hydrogenation to Methanol under the Real Reaction Conditions. *J. CO2 Util.* **2020**, *37*, 55–64.
(40) Jehng, J. M.; Wachs, I. E.; Patience, G. S.; Dai, Y. M. Experimental Methods in Chemical Engineering: Temperature Programmed Surface Reaction Spectroscopy—TPSR. *Can. J. Chem. Eng.* **2021**, *99* (2), 423–434.
(41) Kokalj, A.; Makino, T.; Okada, M. DFT and TPD Study of the Role of Steps in the Adsorption of CO on Copper: Cu(4 1 0) versus Cu(1 0 0). *J. Phys.:Condens. Matter* **2017**, *29* (19), No. 194001.
(42) Svintsitskiy, D. A.; Kardash, T. Y.; Stonkus, O. A.; Slavinskaya, E. M.; Stadnichenko, A. I.; Koscheev, S. V.; Chupakhin, A. P.; Boronin, A. I. In Situ XRD, XPS, TEM, and TPR Study of Highly Active in Co Oxidation CuO Nanopowders. *J. Phys. Chem. C* **2013**, *117* (28), 14588–14599.
(43) Lin, R.; Luo, M. F.; Xie, Y. L.; Zhong, Y. J.; Liu, W. P. TPD, TPR study and catalytic activity of $CuO/Ce_{0.7}Sn_{0.3}O_2$ catalysts for low-temperature CO oxidation. *React. Kinet. Catal. Lett.* **2004**, *81* (1), 65–71.
(44) Il'ichev, A. N.; Firsova, A. A.; Korchak, V. N. Mechanism of CO Oxidation in Excess H_2 over CuO/CeO_2 Catalysts: ESR and TPD Studies. *Kinet. Catal.* **2006**, *47* (4), 585–592.
(45) Avgouropoulos, G.; Ioannides, T. TPD and TPSR Study of CO Interaction with $CuO\text{-}CeO_2$ Catalysts. *J. Mol. Catal. A:Chem.* **2008**, *296* (1–2), 47–53.
(46) Uzunova, E. L.; Seriani, N.; Mikosch, H. CO_2 Conversion to Methanol on Cu(I) Oxide Nanolayers and Clusters: An Electronic Structure Insight into the Reaction Mechanism. *Phys. Chem. Chem. Phys.* **2015**, *17* (16), 11088–11094.
(47) Arenal, R.; Peña, F.; de laStéphan, O.; Walls, M.; Tencé, M.; Loiseau, A.; Colliex, C. Extending the Analysis of EELS Spectrum-Imaging Data, from Elemental to Bond Mapping in Complex Nanostructures. *Ultramicroscopy* **2008**, *109* (1), 32–38.
(48) Liang, H.; Zhang, G.; Li, Z.; Zhang, Y.; Fu, P. Catalytic Hydrogenation of CO_2 to Methanol over Cu-Based Catalysts: Active Sites Profiling and Regulation Strategy as Well as Reaction Pathway Exploration. *Fuel Process. Technol.* **2023**, *252*, No. 107995.
(49) Al Abdulghani, A. J.; Ganguly, S.; Hagmann, R. H.; Sun, Z.; Alvear, M.; Mark, L. O.; Nikolla, E.; Pagán-Torres, Y. J.; Hermans, I. Uncovering the Pressure-Dependent Mechanism of CO_2 Hydrogenation to Methanol on Ga-Promoted Cu/ZrO_2 Using Operando Modulation-Excitation DRIFTS. *J. Am. Chem. Soc.* **2025**, *147* (31), 27438–27448.
(50) Chen, H.; Fan, T.; Ji, Y. CO_2 Reduction Mechanism on the $Cu_2O(110)$ Surface: A First-Principles Study. *ChemPhysChem* **2023**, *24* (11), No. e202300047.
(51) Challiwala, M. S.; Ghouri, M. M.; Linke, P.; El-Halwagi, M. M.; Elbashir, N. O. A Combined Thermo-Kinetic Analysis of Various Methane Reforming Technologies: Comparison with Dry Reforming. *J. CO2 Util.* **2017**, *17*, 99–111.
(52) Jurado A, D. A.; Higham, M. D.; Poh, Y. R.; Catlow, C. R. A.; Krossing, I. Mechanism of CO_2 Conversion to Methanol on a Highly Representative Model Cu/ZnO Interface. *J. Catal.* **2025**, *446*, No. 115997.
(53) Yang, Y.; Mims, C. A.; Mei, D. H.; Peden, C. H. F.; Campbell, C. T. Mechanistic Studies of Methanol Synthesis over Cu from $CO/CO_2/H_2/H_2O$ Mixtures: The Source of C in Methanol and the Role of Water. *J. Catal.* **2013**, *298*, 10–17.
(54) Chinchen, G. C.; Spencer, M. S.; Waught, K. C.; Whan, D. A. Promotion of Methanol Synthesis and the Water-Gas Shift Reactions by Adsorbed Oxygen on Supported Copper Catalysts. *J. Chem. Soc., Faraday Trans. 1* **1987**, *1* (83), 2193–2212.
(55) Lee, J. S.; Lee, K. H.; Lee, S. Y.; Kim, Y. G. A Comparative Study of Methanol Synthesis from CO_2/H_2 and CO/H_2 over a $Cu/ZnO/Al_2O_3$ Catalyst. *J. Catal.* **1993**, *144*, 414–424.
(56) Sahibzada, M.; Metcalfe, I. S.; Chadwick, D. Methanol Synthesis from $CO/CO_2/H_2$ over $Cu/ZnO/Al_2O_3$ at Differential and Finite Conversions. *J. Catal.* **1998**, *174*, 111–118.
(57) Nerlov, J.; Chorkendorff, I. Methanol Synthesis from CO_2, CO, and H_2 over Cu(100) and Ni/Cu(100). *J. Catal.* **1999**, *181*, 271–279.

Downloaded from pubs.acs.org/acscacs/article-pdf/16/12/11604/6430569/cs-2026-029073.pdf by CADIZ UNIV user on 22 October 2026

https://doi.org/10.1021/acscatal.6c02907
ACS Catal. 2026, 16, 11604–11617

(58) Zander, S.; Kunkes, E. L.; Schuster, M. E.; Schumann, J.; Weinberg, G.; Teschner, D.; Jacobsen, N.; Schlögl, R.; Behrens, M. The Role of the Oxide Component in the Development of Copper Composite Catalysts for Methanol Synthesis. *Angew. Chem., Int. Ed.* **2013**, *52* (25), 6536–6540.
(59) Studt, F.; Behrens, M.; Kunkes, E. L.; Thomas, N.; Zander, S.; Tarasov, A.; Schumann, J.; Frei, E.; Varley, J. B.; Abild-Pedersen, F.; Nørskov, J. K.; Schlögl, R. The Mechanism of CO and CO_2 Hydrogenation to Methanol over Cu-Based Catalysts. *ChemCatChem* **2015**, *7* (7), 1105–1111.
(60) Nielsen, N. D.; Thrane, J.; Jensen, A. D.; Christensen, J. M. Bifunctional Synergy in CO Hydrogenation to Methanol with Supported Cu. *Catal. Lett.* **2020**, *150* (5), 1427–1433.
(61) Nielsen, N. D.; Jensen, A. D.; Christensen, J. M. The Roles of CO and CO_2 in High Pressure Methanol Synthesis over Cu-Based Catalysts. *J. Catal.* **2021**, *393*, 324–334.
(62) Martin, O.; Pérez-Ramírez, J. New and Revisited Insights into the Promotion of Methanol Synthesis Catalysts by CO_2. *Catal. Sci. Technol.* **2013**, *3* (12), 3343–3352.
(63) Kresse, G.; Furthmüller, J. Efficiency of Ab-Initio Total Energy Calculations for Metals and Semiconductors Using a Plane-Wave Basis Set. *Comput. Mater. Sci.* **1996**, *6*, 15–50.
(64) Kresse, G.; Furthmüller, J. Efficient Iterative Schemes for Ab Initio Total-Energy Calculations Using a Plane-Wave Basis Set. *Phys. Rev. B* **1996**, *54* (16), 11169–11186.
(65) Perdew, J. P.; Burke, K.; Ernzerhof, M. Generalized Gradient Approximation Made Simple. *Phys. Rev. Lett.* **1996**, *77* (18), 3865–3868.
(66) Kohn, W.; Sham, L. J. Self-Consistent Equations Including Exchange and Correlation Effects. *Phys. Rev.* **1965**, *140* (4A), A1133–A1138.

Downloaded from pubs.acs.org/accacs/article-pdf/16/12/11604/6430569/cs-2026-029073.pdf by CADIZ UNIV user on 22 October 2026

https://doi.org/10.1021/acscatal.6c02907
ACS Catal. 2026, 16, 11604–11617